Effects of grain-to-grain interactions on hear strain localization in Al-Cu-Li rolled sheets

V. Taupin, J. Chevy, Claude Fressengeas

▶ **To cite this version:**

V. Taupin, J. Chevy, Claude Fressengeas. Effects of grain-to-grain interactions on hear strain localization in Al-Cu-Li rolled sheets. International Journal of Solids and Structures, 2016, 99, pp.71-81. 10.1016/j.ijsolstr.2016.07.023 . hal-02935792

HAL Id: hal-02935792

https://hal.univ-lorraine.fr/hal-02935792

Submitted on 10 Sep 2020

HAL is a multi-disciplinary open access archive for the deposit and dissemination of scientific research documents, whether they are published or not. The documents may come from teaching and research institutions in France or abroad, or from public or private research centers.

L'archive ouverte pluridisciplinaire **HAL**, est destinée au dépôt et à la diffusion de documents scientifiques de niveau recherche, publiés ou non, émanant des établissements d'enseignement et de recherche français ou étrangers, des laboratoires publics ou privés.

Effects of grain-to-grain interactions on hear strain localization in Al-Cu-Li rolled sheets

[1]V. Taupin, [2]J. Chevy, [1*]C. Fressengeas

[1] *Laboratoire d'Etude des Microstructures et de Mécanique des Matériaux, Université de Lorraine/CNRS, Ile du Saulcy, 57045 Metz Cedex, France*
[2] *Constellium Technology Center, 725 Rue Aristide Bergès, 38341 Voreppe, France*

Abstract

Crystal plasticity finite element simulations of tensile tests on thin polycrystalline samples with grain orientations representative of the microstructure in Al-Cu-Li rolled sheets are carried out to study the influence of grain-to-grain interactions on plastic strain localization. Anisotropic work-hardening and rate-sensitivity of the material behavior are assumed. The grains are modeled as thin platelets in the through-thickness direction, elongated in the rolling and transverse directions. The only distinctive feature of the present simulations with respect to standard crystal plasticity calculations is the enforcement of tangential continuity conditions on the elastic and plastic distortion rates along grain boundaries, which introduces grain-to-grain interactions and renders the simulations nonlocal. Whereas standard crystal plasticity calculations do not predict any significant plastic strain pattern, slanted shear bands spontaneously emerge throughout the sample in the simulations involving tangential continuity, in agreement with experimental observations. Also in agreement with experimental data, shear banding is delayed when the tensile axis shifts from rolling to transverse direction, and the trend to shear banding is enhanced when grain thickness is decreased, particularly in loading along the rolling direction.

*Corresponding author: claude.fressengeas@univ-lorraine.fr

1. Introduction

New Al-Cu-Li alloys have been recently developed to meet air framers requirements. In addition to their low density, they offer an excellent corrosion resistance and a combination of specific yield strength and damage tolerance properties (fracture toughness and fatigue crack growth resistance), weldability and formability, that is not achieved in conventional alloys (Lavernia,1987; Heinz,2000; Warner,2006; Alexopoulos,2013). Hence, they appear as promising candidates for weight-saving strategies in the aerospace industry. One crucial challenge regarding these alloys is to understand the complex relationships that exist between their material properties in the processed sheets (yield strength, work hardening characteristics, morphological and crystallographic textures, solute and precipitation conditions, etc.) and the ductility of these sheets. Extensive experimental and theoretical efforts have been aimed at elucidating this relationship (Besson,2001; Xue,2007; Chen,2011; Morgeneyer,2011; Beaudoin,2013; Morgeneyer,2014; Zhang,2014; Messner,2014; Messner,2015; Ovri,2015a). In particular, in-situ monitoring of precursor damage/void and strain fields was performed in notched samples during Kahn tear tests in thin AA-2198 sheets (Morgeneyer,2014). Tensile loading was applied in the rolling direction L, the notch faces were in the transverse-through-thickness plane (T,S) and the notch front in the through-thickness direction S, which defines the so-called L-T configuration of the sample. It was observed that developing cracks are not influenced by damage/void features that possibly nucleate at the earliest steps of the process, although this is usually expected in notched samples, which favor dimple fracture, and in plane-stress conditions (Broek,1974). Instead, fracture occurred along transgranular paths lying in the (L,S) back-side of the sample (opposite to the notch) within rather straight slanted through-sample shear bands formed after a flat-to-slant transition. Such observations unambiguously suggest that plastic shear banding is a precursor to failure in these alloys. Hence, we are inclined to believe that modeling studies aimed at ductility predictions in Al-Cu-Li alloys should be devoted to the onset and development of plastic strain localization phenomena in the first place, before turning to investigations of the failure mechanisms.

Standard crystal plasticity finite element (CPFE) simulations of the Kahn tear test in a work hardening material were found unable to predict shear banding (Morgeneyer,2014). Even additionally introducing damage soften-

ing in the model material did not allow capturing the emergence of slanted shear bands, although such modeling can reproduce the flat-to-slant fracture transition in cases where the crack path follows earlier damage features (Besson,2001; Xue,2007; Morgeneyer,2011). Interestingly, recent 3D CPFE simulations of polycrystalline copper samples submitted to rolling predicted the occurrence of transgranular shear bands although the material did not present softening behavior (Knezevic,2014a). This feature was obtained by explicitly meshing the grain structure and grain boundary surfaces, thus presumably accounting in a better way for grain-to-grain interactions. Similar treatment of the plane strain compression of a two-phase hexagonal closed-packed/body-centered cubic Zr/Nb layered composite captured the occurrence of shear strain localization, but full-fledged shear band development required introducing an additional softening mechanism (Ardeljan,2015). In the present paper, we intend to perform 3D CPFE simulations of the tensile loading of geometrically perfect parallelepipedic slabs of an anisotropic work-hardening material, that also include a careful treatment of grain boundaries (but different in nature from (Knezevic,2014a)) to show that grain-to-grain interactions decisively contribute to the occurrence of shear banding in such materials. We note here that, depending on precipitation/solute conditions, solute softening may well occur and contribute to plastic strain localization in Al-Cu-Li alloys (Delafosse,1993; Zhang,2014; Ovri,2015b). However, such effects are presently overlooked in order to restrict the paper to the treatment of what we see as a key preliminary issue in this problem. Our motivation for these simulations stems from recent work showing that, in addition to tangential continuity of the *total* distortion and distortion rate tensors at grain boundaries, which ensures the continuity of matter (Hadamard,1903), tangential continuity of the *elastic* and *plastic* distortion and distortion rate tensors needs to be satisfied along grain boundaries to avoid undue elastic/plastic incompatibility and for consistency of continuous modeling (Acharya,2007; Fressengeas,2012). Usually overlooked in standard CPFE calculations, these tangential continuity conditions lead to long-range nonlocal interactions between adjacent grains, which promote the Bauschinger effect and the development of heterogenous plastic strain fields in their neighborhood, (Richeton,2011; Taupin,2015) and lead to improved predictions of texture evolution (Mach,2010). Our modeling paradigm in Al-Cu-Li alloys is that, due to their strongly multi-layered morphological texture, tangential continuity of the elastic/plastic distortion rates turns out to be the key factor for the emergence of transgranular strain localization

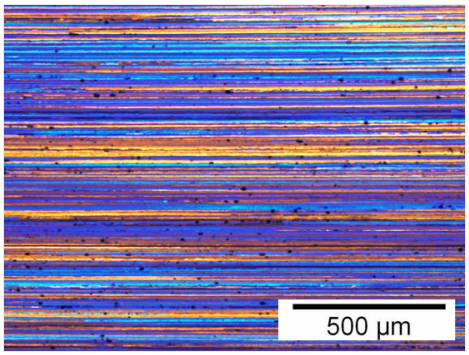

Figure 1: Microstructure of the $4.2mm$ sheet in the L-S plane. The rolling L and through-thickness S directions are horizontal and vertical, respectively.

patterns, and helps to explain grain size and crystallographic texture effects on the development of through-sample shear bands. As already indicated above, we postpone for future work detailed studies on how and when shear bands give way to crack nucleation and growth in these alloys, by using modeling ideas developed in (Fressengeas,2014; Fressengeas,2016) on concurrent plastic straining and crack development.

The plan of the paper is as follows. In Section 2, we present the experimental data collected from Al-Cu-Li sheet samples deformed in simple tension in the L and T directions. Different sheet thicknesses obtained through different processing routes are tested. In Section 3, we present the CPFE framework used in the tensile loading simulations. In Section 4, the concepts of geometrically necessary dislocation density and lattice incompatibility are recalled to help introduce the tangential continuity conditions at interfaces presented in Section 5, where we show in addition how to incorporate these conditions in a standard CPFE setting. In Section 6, we provide simulation results for Al-Li-Cu samples loaded in the L and T directions, with and without tangential continuity conditions, and we analyse the effects of grain and sheet thickness, in comparison with the experimental data. A discussion section closes the paper. The notations are provided in Appendix A.

Table 1: Experimental grain orientations (with variants) and volume fractions f (in percent). The Euler angles (ϕ_1, ϕ, ϕ_2) (in $^\circ$) provide the orientation of the crystal with respect to the rolling frame (L,T,S).

$Orientation$	$\phi 1$	ϕ	ϕ_2	f
$brass-a$	54.74	90.0	45.0	
$brass-b$	35.26	45.0	0.0	30
$S-a$	-58.98	36.7	26.57	
$S-b$	121.02	36.7	26.57	
$S-c$	58.98	143.3	26.57	
$S-d$	-121.02	143.3	26.57	50
$copper-a$	90.0	35.26	45.0	
$copper-b$	39.23	65.9	26.56	10
$cube$	0.0	0.0	0.0	
$Goss$	0.0	45.0	0.0	10

Table 2: Tensile properties for various sheet thicknesses and loading directions: Tensile Yield Stress, Ultimate Tensile Strength and Elongation at failure.

$Thickness(mm)$	$Loading\,direction$	$TYS\,(MPa)$	$UTS\,(MPa)$	$E\,\%$
2.5	L	403	446	11.6
2.5	T	378	419	16.2
4.2	L	391	436	13.4
4.2	T	373	416	17.1

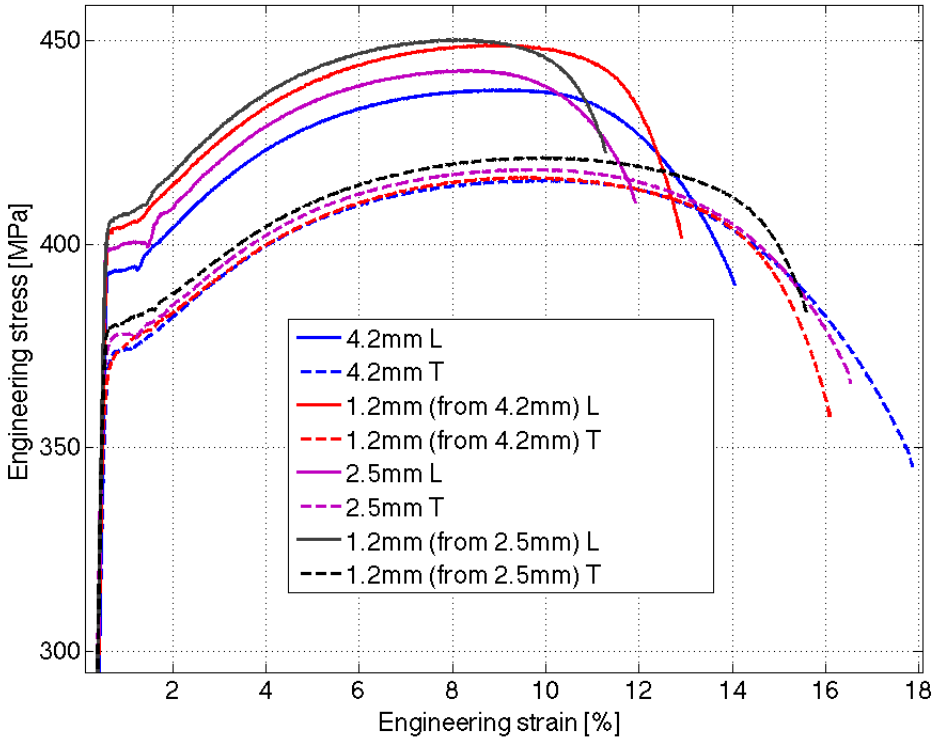

Figure 2: Tensile tests on samples along L and T directions for different thicknesses. Engineering stress (MPa) vs. engineering strain (%). The $1.2mm$-thick samples were obtained by further machining the $2.5mm$ and $4.2mm$-thick rolled sheets.

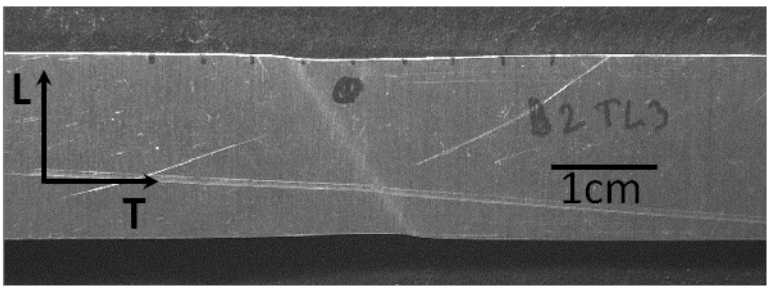

Figure 3: Shear band traversing a sample in the necking region for tensile loading along the T-direction up to 10% strain. Grains are distinctly elongated along the L-direction, normal to the tensile axis. The sample is $1.2mm$-thick and is obtained by machining a $2.5mm$-thick rolled sheet (black dashed line in Fig.2).

2. Experimental data in Al-Cu-Li alloys

The material used in this study has a composition that is very close to the Al-Cu-Li alloy AA-2198. It has been industrially processed into sheets of thickness 2.5 and $4.2mm$. Processing routes include rolling and several thermo-mechanical heat-treatments that lead to multi-layered morphological textures with grains strongly elongated in the rolling direction L, as illustrated in Fig.1, and to the precipitation of hardening phases (artificial aging). Machining may be used to reduce further the sheet thickness while keeping the grain thickness constant. Orientation maps of the sheets have been obtained by means of X-ray diffraction analysis. The average volume fractions of the main texture components are reported in Table 1. Tensile tests have been carried out using the as-delivered $2.5mm$ and $4.2mm$ thickness sheets, as well as samples that have been machined down to $1.2mm$ from these two initial thicknesses. The thickness, width and gauge-length of the samples were $(2.5mm, 18mm, 53mm)$, $(4.2mm, 18mm, 53mm)$ and $(1.2mm, 18mm, 48mm)$. In each case, samples have been loaded in both the rolling L and transverse T direction. Typical nominal stress-tensile strain curves are shown in Fig.2. Failure of the samples occurred while the load was decreasing after the nominal Ultimate Tensile Strength (UTS), and moderate necking was observed, particularly when loading in the L direction. The samples failed along shear bands forming across the samples in the necking areas (see Fig.3). The shear bands were at angle with the loading direction and slanted in the sample cross-section. Mean values of the characteristic

tensile properties obtained from three independent tests for each configuration (thickness and loading direction) are reported in Table 2. Several trends can be identified in this table and in Fig.2:
(i) The elongation to failure E and post-UTS elongation to failure are significantly lower when the material is loaded in the L direction than in the T direction, which is uncommon in Al-based rolled sheets.
(ii) The elongation to failure E slightly decreases when the sheet thickness is reduced by machining, *i.e.*, at constant grain thickness.
(iii) The elongation to failure E decreases significantly when the sheet thickness is reduced by rolling, *i.e.*, by also decreasing grain thickness, and the trend is stronger in L loading than in T loading.
(iv) The Tensile Yield Strength (TYS) and UTS are larger when the samples are loaded in the rolling direction L than in the transverse direction T.

Anisotropy of the TYS is mostly due to the fact that the forming process includes an additional tensile pre-strain in the L direction. Provisionally, no attempt is made at interpreting the anisotropy of the UTS in this paper, although hints will be given in Section 7. Only the issues (i) through (iii) will be discussed. Note first that, like the Kahn test samples, our tensile samples are close to plane stress state. Hence, the stress-triaxiality factor, the damage nucleation rate and trend to dimple fracture are expected to be similar. The trend (i) of the elongation to failure in the tensile samples is inconsistent with the void nucleation, growth and coalescence mechanism. Since damage initiation sites, such as intermetallic particles, are aligned in the L direction, crack growth should be promoted in this direction, which is more expected in tensile samples when they are loaded in the T direction. Hence, the elongation to failure should be smaller when loading the samples in this direction, which is inconsistent with trend (i). It is therefore believed that earlier failure in the L direction is indication that another fracture mechanism is involved. Indeed, as mentioned above, careful examination of the necking area revealed shear bands extending throughout the sample and failure of the sample along these bands. The intent of the modeling approach detailed in the next three sections is to show that, in contrast with conventional CPFE modeling, the account of grain-to-grain interactions through tangential continuity of the plastic distortion rate across grain boundaries allows predicting plastic strain fields that are consistent with the trends (i) through (iii).

3. Crystal plasticity finite element model

In a small strain setting, we consider the elasto-plastic deformation of a body B subjected to external displacements $\mathbf{u}$ and tractions $\mathbf{t}$ on its external boundaries ∂B_u and ∂B_t. In the absence of body forces, the momentum equation reduces to:

$$\mathbf{div}\,\mathbf{T} = 0, \tag{1}$$

where $\mathbf{T}$ denotes the symmetric Cauchy stress tensor. Homogeneous linear isotropic elasticity can be reasonably assumed for an Al-based alloy:

$$T_{ij} = \lambda \epsilon^e_{kk} \delta_{ij} + 2\mu \epsilon^e_{ij}, \tag{2}$$

where λ and μ are the Lamé constants. The the elastic strain tensor is $\boldsymbol{\epsilon}_e = \boldsymbol{\epsilon} - \boldsymbol{\epsilon}_p$, where $\boldsymbol{\epsilon}$ and $\boldsymbol{\epsilon}_p$ are respectively the total and plastic strain tensors. In the crystal plasticity model chosen here (Richeton,2011), the evolution of the plastic strain tensor is provided by incrementing the symmetric part of the plastic distortion rate tensor $\dot{\mathbf{U}}_p$, which can be identified with the plastic slip rate tensor $\mathbf{L}_p$ in standard crystal plasticity:

$$\mathbf{L}_p = \sum_s \rho^m_s b v_s \mathbf{m}_s \otimes \mathbf{n}_s = \sum_s \dot{\gamma}^p_s \boldsymbol{P}_s \tag{3}$$

$$\dot{\boldsymbol{\epsilon}}_p = \mathbf{L}^{sym}_p. \tag{4}$$

Here, $\dot{\gamma}^p_s = \rho^m_s b v_s$ is the plastic slip rate on slip plane s of slip direction $\mathbf{m}_s$ and normal $\mathbf{n}_s$ produced by the mobile dislocation density ρ^m_s of average velocity v_s. The magnitude of the Burgers vector of all slip systems is b. $\mathbf{P}_s = \mathbf{m}_s \otimes \mathbf{n}_s$ is the orientation Schmid tensor. Dislocation glide on system s is activated by the resolved shear stress $\tau_s = \mathbf{T} : \mathbf{P}_s$ through the power law relationship

$$v_s = v_0 \left(\frac{|\tau_s|}{\tau^h_s + \tau_p} \right)^n sign(\tau_s), \tag{5}$$

where v_0 and n are a reference velocity and the rate sensitivity exponent, respectively. Particle hardening is accounted for by the constant stress τ_p and τ^h_s represents forest hardening on slip system s. Latent hardening is assumed in the form:

$$\tau_s^h = \mu b \sqrt{\sum_j a_{js} \rho_j^f}, \tag{6}$$

where the latent hardening coefficient a_{js} is assigned to the contribution of the forest density ρ_j^f on slip system j to hardening of slip system s. A mean value a_{mean} is taken for all these coefficients, except for collinear interactions where the value a_{col} is used. The rates of evolution of the mobile and forest dislocation densities in slip system s read

$$\frac{\dot{\rho}_s^m}{\rho^{m0}} = \left(K_m - K_f + \frac{C_1}{\sqrt{\rho^{m0}}} \sum_j \sqrt{\rho_j^f} - \frac{C_2}{\rho^{m0}} \sum_j \sqrt{\rho_s^m \rho_j^f} \right) |\dot{\gamma}_s^p|, \tag{7}$$

$$\frac{\dot{\rho}_s^f}{\rho^{f0}} = \left(K_f + \frac{C_2}{\rho^{m0}} \sum_j \sqrt{\rho_s^m \rho_j^f} - \frac{C_3}{\rho^{m0}} \rho_s^f \right) |\dot{\gamma}_s^p|. \tag{8}$$

In the above, K_m and K_f reflect mobile and forest dislocation source terms, C_1, C_2 and C_3 account respectively for the contribution of forest dislocation to mobile dislocation sources, the arrest of mobile dislocations due to interactions with forest dislocations and dynamic recovery. All material parameters are listed in Table 3. They are generic for Al-based alloys, and no attempt is made at fitting the parameters for the particular alloy we used in our experiments. Similarly, the latent hardening coefficients are deliberatly taken from previous work on Al alloys (Richeton,2011). The unknown field of the boundary value problem is the total displacement field. It is obtained from the solution of the set of field equations (1-8) and standard boundary conditions on traction and displacement vector fields.

4. Lattice incompatibility and geometrically necessary dislocation densities

Let the tensors $\mathbf{U}_e$ and $\mathbf{U}_p$ be respectively the elastic and plastic distortion tensors, whose symmetric parts are the elastic and plastic strain tensors defined above. Let us consider a mesoscale closed circuit C bounding a patch S of unit normal $\mathbf{n}$. An ensemble $\mathcal{E}$ of dislocation lines may be threading S (see Fig.4). Two cases are now being considered. (i) If the net Burgers vector $\mathbf{b}$ of the ensemble $\mathcal{E}$ cancels, the dislocation density reflecting $\mathcal{E}$ is referred

Table 3: Numerical constants used for generic Al-based alloys.

n	v_0	ρ^{m0}	ρ^{f0}	a_{mean}	a_{col}	b
10	$7\,10^{-10} m/s$	$2\,10^{12} m^{-2}$	$2\,10^{12} m^{-2}$	0.12	1.265	$0.286 nm$
K_m	K_f	C_1	C_2	C_3		
$2.8\,10^4$	$1.4\,10^4$	$2.2\,10^3$	80	500		
λ	μ	τ^p				
$62 GPa$	$23 GPa$	$25 MPa$				

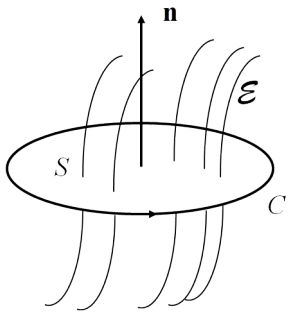

Figure 4: Schematic showing closed circuit C bounding a patch S of unit normal $\mathbf{n}$, threaded by dislocation ensemble $\mathcal{E}$.

to as a "statistical dislocation density". This quantity does not produce lattice incompatibility, in the sense that no discontinuity of the elastic/plastic displacement can be detected at the scale of surface S. (ii) If instead the net Burgers vector $\mathbf{b}$ of ensemble $\mathcal{E}$ is non zero, it represents a discontinuity of the elastic/plastic displacement, which induces incompatibility of the elastic distortion at this scale. The net Burgers vector $\mathbf{b}$ can be obtained by integrating the elastic distortion along circuit C:

$$\mathbf{b} = \int_C \mathbf{U}_e \cdot \mathbf{dr}. \tag{9}$$

The Burgers vector is a point-wise measure of lattice incompatibility over surface S. The continuous density that is associated with this incompatibility is the geometrically necessary dislocation density tensor $\boldsymbol{\alpha}$, also referred to as the polar or excess dislocation density tensor (Nye,1953). In a cartesian reference frame $(\mathbf{e_1}, \mathbf{e_2}, \mathbf{e_3})$, its component $\alpha_{ij} = b_i\, t_j$ is formed from the

net Burgers vector component in direction $\mathbf{e_i}$ per unit surface S, b_i, and the component along $\mathbf{e_j}$, t_j, of the line vector. Using this definition, the net Burgers vector can be expressed as

$$\mathbf{b} = \int_S \boldsymbol{\alpha} \cdot \mathbf{n} dS. \tag{10}$$

Applying now the Stokes's theorem to Eq.(9) and comparing with Eq.(10) yields the well-known incompatibility equation (Kröner,1980):

$$\mathbf{curl} \mathbf{U}_e = \boldsymbol{\alpha}. \tag{11}$$

The above equation implies that non-vanishing geometrically necessary dislocation densities are associated with an incompatible non-gradient part $\mathbf{U}_\mathbf{e}^\perp$ of the elastic distortion, whose curl is non-zero. Because the *total* distortion is a compatible gradient curl-free tensor, an incompatible part $\mathbf{U}_p^\perp$ of the *plastic* distortion must exist and offset the incompatible part $\mathbf{U}_e^\perp$ of the *elastic* distortion. Hence, the following relations are satisfied :

$$\begin{aligned}
\mathbf{U}_e &= \mathbf{U}_e^\perp + \mathbf{U}_e^\parallel && (12)\\
\mathbf{U}_p &= \mathbf{U}_p^\perp + \mathbf{U}_p^\parallel && (13)\\
0 &= \mathbf{U}_e^\perp + \mathbf{U}_p^\perp && (14)\\
\mathbf{curl}\, \mathbf{U}_e^\perp &= -\mathbf{curl}\, \mathbf{U}_p^\perp = \boldsymbol{\alpha} \neq 0. && (15)
\end{aligned}$$

In the above, the compatible plastic component, $\mathbf{U}_p^\parallel$, is built from compatible plastic distortion increments and the compatible elastic component, $\mathbf{U}_e^\parallel$, allows to ensure the balance of momentum and satisfaction of boundary conditions (Acharya,2001). Because it will be employed to implement the forthcoming tangential continuity conditions, the method used to determine in a unique way the incompatible plastic (or elastic, up to a sign) distortion existing in the presence of a prescribed tensor field $\boldsymbol{\alpha}$ is now recalled (Acharya,2004). Indeed, the Stokes-Helmholtz decomposition is employed to split uniquely the elastic and plastic distortions into incompatible grad-free and compatible curl-free parts:

$$\mathbf{U}_e = \mathbf{U}_e^{\perp} + \mathbf{U}_e^{\parallel} = \mathbf{curl}\boldsymbol{\chi} + \mathbf{grad}\,\mathbf{w}, \quad (16)$$

$$\mathbf{U}_p = \mathbf{U}_p^{\perp} + \mathbf{U}_p^{\parallel} = -\mathbf{curl}\boldsymbol{\chi} + \mathbf{grad}\,\mathbf{z}, \quad (17)$$

in such a manner that their sum, the total distortion, is a gradient tensor. Taking the curl of the above relations extracts the curl parts, whereas taking their divergence extracts the gradient parts. The incompatible plastic distortion $\mathbf{U}_p^{\perp}$ is solution of Eq.(15). To ensure that $\mathbf{U}_p^{\perp}$ is unique and does not contain a gradient part, and further that it actually vanishes when $\boldsymbol{\alpha} = 0$, one has to append the side conditions:

$$\mathbf{div}\,\mathbf{U}_p^{\perp} = 0 \quad (18)$$

$$\mathbf{U}_p^{\perp} \cdot \mathbf{n} = 0 \quad on\ \partial B \quad (19)$$

to Eq.(15). Then, performing the curl of both the left and right hand sides of this equation yields

$$\mathbf{curl}\left(\mathbf{curl}\mathbf{U}_p^{\perp}\right) = \mathbf{grad}\left(\mathbf{div}\mathbf{U}_p^{\perp}\right) - \mathbf{div}\left(\mathbf{grad}\mathbf{U}_p^{\perp}\right) = -\mathbf{curl}\boldsymbol{\alpha}, \quad (20)$$

and taking account of Eq.(18) in the latter leads to

$$\mathbf{div}\left(\mathbf{grad}\mathbf{U}_p^{\perp}\right) = \mathbf{curl}\boldsymbol{\alpha}. \quad (21)$$

Thus, each component of $\mathbf{U}_p^{\perp}$ is solution of the Poisson equation

$$U_{ij,rr}^{p,\perp} = e_{jkl}\alpha_{il,k}, \quad (22)$$

under the boundary conditions (19). Hence, uniqueness is guaranteed and it is found in particular that $\mathbf{U}_p^{\perp} = 0$ when $\boldsymbol{\alpha} = 0$, as required. Eqs.(21,22) can be solved by using finite element weak form approximations (Hecht,2012; Taupin,2015) or by Fast Fourier Transform methods (Berbenni,2014). Finite elements will be used in the following section to enforce the tangential continuity conditions. Note finally that, because the curl operator leaves aside the compatible part of $\mathbf{U}_p$, Eq.(15) can also be written as $-\mathbf{curl}\,\mathbf{U}_p = \boldsymbol{\alpha}$. Taking the time derivative yields :

$$\dot{\boldsymbol{\alpha}} = -\mathbf{curl}\,\dot{\mathbf{U}}_p = -\mathbf{curl}\,\mathbf{L}_p. \quad (23)$$

This rate equation is sometimes used in crystal plasticity models as part of a post-treatment procedure for updating the geometrically necessary dislocation density tensor, after the set of equations (1-8) for the displacement field has been solved. However, as we show in the next Section, the geometrically necessary dislocation density requires specific treatment at grain boundaries, and this procedure needs to be further discussed.

5. Tangential continuity of elastic and plastic distortions at interfaces

In this Section, motivations for satisfying tangential continuity conditions on the elastic/plastic distortion and distortion rate tensors at interfaces (Acharya,2007), and a derivation of the latter are provided for the sake of completeness. We have in mind a mesoscale representation of polycrystals where the spatial resolution length scale is not sufficiently small to reveal the core structure of grain boundaries. The latter are therefore seen as interfaces of vanishingly small thickness, across which the lattice rotation and possibly plastic distortion and distortion rate components experience a discontinuity. Let us consider two grains A and B, bounded by such a singular interface (I) of unit normal $\mathbf{n}$ oriented from grain A towards grain B at point P. The discontinuity of tensor $\mathbf{W}$ at the interface is denoted $[\![\mathbf{W}]\!] = \mathbf{W}_B - \mathbf{W}_A$. Using the definitions (9,10) of the net Burgers vector, and collapsing the circuit C onto a point P of the interface, yields:

$$\forall \mathbf{l},\ [\![\mathbf{U}_e]\!].\mathbf{l} = \boldsymbol{\alpha}^S(I).\mathbf{t}, \tag{24}$$

where the unit vectors $\mathbf{l}$ and $\mathbf{t} = \mathbf{n} \times \mathbf{l}$ belong to the interface, and form an orthonormal basis with $\mathbf{n}$. The above equation is nothing but the celebrated Frank-Bilby interfacial relation (Frank,1950; Bilby,1955). It means that, whatever the tangential discontinuity of the elastic distortion, there exists a surface dislocation density $\boldsymbol{\alpha}^S(I)$ that accommodates this discontinuity. This equation is equivalent to the interfacial version of Eq.(15), which reads in component form :

$$\alpha^S_{ij}(I) = e_{jkl}[\![U^e_{il}]\!]\ n_k. \tag{25}$$

The above relation was also proposed in (Bilby,1955). It applies as well, up

to a sign, to the plastic distortion and plastic distortion rate:

$$\alpha_{ij}^S(I) = -e_{jkl}[\![U_{il}^p]\!]\, n_k, \tag{26}$$

$$\dot{\alpha}_{ij}^S(I) = -e_{jkl}[\![\dot{U}_{il}^p]\!]\, n_k, \tag{27}$$

because the total distortion satisfies tangential continuity conditions, known as Hadamard compatibility conditions (Hadamard,1903). It is essential for what follows to realize that $\boldsymbol{\alpha}^S(I)$ is a mathematical object of a different nature from the dislocation density tensor $\boldsymbol{\alpha}$. Whereas $\boldsymbol{\alpha}$ (expressed in units of Burgers vector length per unit surface) is a continuously defined field in the bulk of the crystal and represents a volumetric dislocation ensemble, the surface dislocation density tensor $\boldsymbol{\alpha}^S(I)$ (in units of Burgers vector length per unit length, *i.e.* non dimensional) is a two-dimensional density field supported by the singular interface I. The surface dislocations model may sometimes be taken more or less literally: electron microscopy has revealed that low angle boundaries or semi-coherent interfaces actually involve interfacial dislocations (Priester,1979; Csiszár,2011). In most cases however, surface dislocations cannot be identified with observable dislocations, and they reduce to being only mathematical artefacts, whose role is to accommodate any existing tangential discontinuity of the elastic distortion across the interface. For example, they do not represent the actual structure of high angle boundaries, because their spacing would be so small that their cores would overlap (Priester,2013). Because their existence as a model goes with the notion of a singular interface, we will assume $\boldsymbol{\alpha}^S(I) = 0$ in the following, in order to distribute the dislocation density arising at grain boundaries over a finite volumetric boundary layer, perhaps of a small thickness - but definitely not vanishingly small. Thus, according to Eq.(24), we set the condition:

$$\forall \mathbf{l} \in I,\ [\![\mathbf{U}_e]\!].\mathbf{l} = 0, \tag{28}$$

whose meaning is that tangential discontinuity of the elastic distortion is rejected. However, normal discontinuity of the elastic distortion remains permitted, which leaves open the possibility for elastic strain and rotation jumps across the interface. Eq.28 is written equivalently as

$$[\![\mathbf{U}_e]\!] \times \mathbf{n} = 0, \tag{29}$$

and similar conditions can be derived for the plastic distortion and distortion

rate tensors:

$$[\![\mathbf{U}_p]\!] \times \mathbf{n} = 0 \tag{30}$$

$$[\![\dot{\mathbf{U}}_p]\!] \times \mathbf{n} = [\![\mathbf{L}_p]\!] \times \mathbf{n} = 0. \tag{31}$$

Therefore, in line with the above, the singular density $\boldsymbol{\alpha}^S(I)$ also appears as a mathematical artefact accommodating any discontinuity of the tangential plastic distortion and distortion rate across the interface. By removing $\boldsymbol{\alpha}^S(I)$, tangential continuity of the latter across the interface and non-locality of the elasto-plastic response of the polycrystal are induced, because values from the left of the interface have to be equal to values from the right. Such non-locality has been shown to have a strong impact on the elastic/plastic strain and rotation fields in the vicinity of grain boundaries. It allowed retrieving such complex features as size effects, loading path-dependency, the Bauschinger effect and directional hardening in the plastic response of particle-reinforced alloys and thin polycrystalline fims (Richeton,2011; Puri,2011), as well as an overall texture intensity and a β fiber that are more consistent with experimental observation in f.c.c. metals than the Taylor models (Mach,2010). As already mentionned, our intent in this paper is to show that tangential continuity of the elastic/plastic distortion rate is also a key factor in the development of transgranular sample-scale localization of strain in shear bands in Al-Li-Cu rolled sheets.

The algorithm used to enforce tangential continuity of the elastic/plastic distortion and distortion rates in CPFE simulations is now detailed (see also (Taupin,2015)). In our code, grain boundaries usually cross mesh elements. In these "boundary" elements, some nodes pertain to one crystal, some to the other. Since all variables are known from their nodal values, it may be stated that the grain boundaries are actually spread out in these elements, over the distance between nodes pertaining to one grain or to the other. Hence, in practice, the interfacial relation (31) is also spread out over this distance and finding $\boldsymbol{\alpha}^S(I)$ is equivalent to incrementing $\boldsymbol{\alpha}$ from Eq.(23). In other words, the geometrically necessary dislocation density $\boldsymbol{\alpha}$ built by using Eq.(23) at nodes on both sides of the boundary reflects the interfacial density $\boldsymbol{\alpha}^S(I)$ spread out over the same nodes. This is precisely the singular density we want to remove, because it accommodates undue tangential discontinuities. Thus, the following algorithm is implemented at each time increment Δt of our explicit code:

(**1**): the stress field being known, compute the plastic slip rate tensor $\mathbf{L}_p$ and update the plastic distortion in the body,
(**2**): compute the increment $\Delta\boldsymbol{\alpha} = \dot{\boldsymbol{\alpha}}\,\Delta t$ in the body through Eq.(23),
(**3**): select the nodes that delimit the grain boundaries and define the increment $\Delta\boldsymbol{\alpha}_I$ that is equal to $\Delta\boldsymbol{\alpha}$ at these boundary nodes, zero elsewhere,
(**4**): update $\boldsymbol{\alpha}$ in the whole body with the increment $\Delta\boldsymbol{\alpha} - \Delta\boldsymbol{\alpha}_I$ (implying that $\boldsymbol{\alpha}$ is set to zero at the boundary nodes),
(**5**): compute the incompatible plastic distortion $\mathbf{U}_p^{\perp,I}$ associated with the increment $\Delta\boldsymbol{\alpha}_I$ by solving Eqs.(21,22) under the boundary conditions (19),
(**6**): remove $\mathbf{U}_p^{\perp,I}$ from the updated value of the plastic distortion in the whole body,
(**7**): update the stress field by solving the balance equation (2) with the adequate boundary conditions, go to step **1**.

As a result of removing the incompatible plastic distortion $\mathbf{U}_p^{\perp,I}$ associated with the surface dislocation density, tangential continuity of the modified plastic distortion is ensured. Because the total distortion is a gradient tensor and necessarily satisfies tangential continuity (Hadamard,1903), the elastic distortion computed as the difference between the total and plastic distortions also satisfies tangential continuity. From the steps (**5**,**6**) of the above algorithm, it can be seen that tangential continuity has a long-range impact. Indeed, removing $\mathbf{U}_p^{\perp,I}$ modifies the plastic distortion in the entire body. In addition, the stress field is modified throughout the body through step **(7)**. In contrast, incrementing $\boldsymbol{\alpha}$ through steps (**1**,**2**) and ignoring steps (**3**-**7**), which is common practice in standard CPFE simulations, yields a dislocation density field localized in the vicinity of interfaces and undue incompatibility of the plastic distortion rate between neighboring grains. In the present interpretation, this dislocation density field appears as a measure of the error made by overlooking tangential continuity of the plastic distortion rate.

6. Simulation results

As already mentioned, the aim in this section is to check whether appending the tangential continuity conditions on the plastic distortion rate (31) to the otherwise conventional CPFE calculations summarized in Section 3, allows retrieving shear strain localization in strongly anisotropic multi-layered polycrystals, as well as the effects of sheet and/or grain thickness, and load-

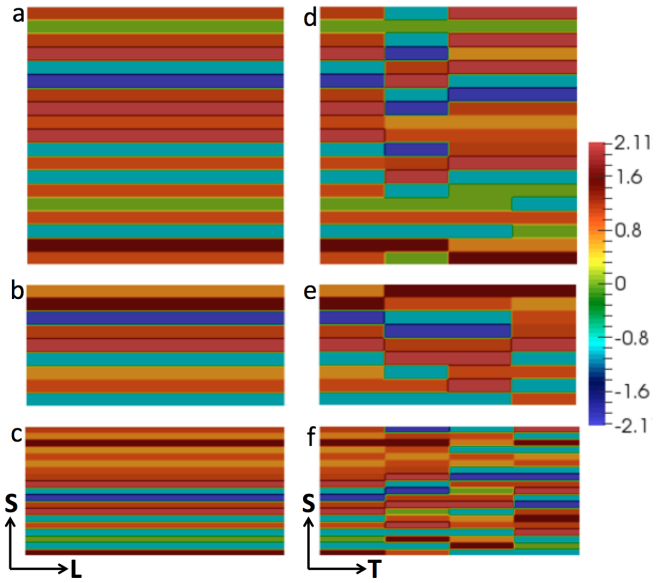

Figure 5: Different sheet microstructures used in the simulations Left: tension along L direction of a slab with (a) 19 grains of thickness 6 μm, (b) 9 grains of thickness $6\mu m$ and (c) 19 grains of thickness $3\mu m$ along the S direction. The rolling frame is shown at the bottom. Right: tension along T direction of a slab with (d) 19 grains of thickness $6\mu m$, (e) 9 grains of thickness $6\mu m$ and (f) 19 grains of thickness $3\mu m$ along the S direction. The rolling frame is shown at the bottom. The color-code is relative to the Euler angle $\phi(rad)$.

ing orientation on strain localization. To this end, we performed 3D simulations of the tensile loading of geometrically perfect parallelepipedic slabs, and made qualitative comparisons with our experimental data and results in (Morgeneyer,2014). The slabs are construed as aggregates of grains modelled as 3D parallelepipeds, with dimensions l, t, s in the L, T and S directions, respectively. It is assumed that $l >> t >> s$ to mimic the anisotropic grain shape produced by rolling. All the initial microstructures we used are shown in Fig.5. In the reference L configuration shown in Fig.5.a, the direction T is normal to the figure, and simple tension is applied along direction L by prescribing displacements in this direction along the (S,T) boundaries, with quasi-static strain rate $10^{-4}s^{-1}$. The (L,T) boundaries of the slab are free surfaces. Periodic conditions are imposed on the (L,S) boundaries, and we assume plane-strain conditions normal to the T direction. Therefore, only a thin slice of material ($1\mu m$ wide) is considered in this direction. The slab is composed of 19 grains of thickness $s = 6\mu m$, so its total thickness is $S = 114\mu m$. Its length in direction L is also $114\mu m$, with only one grain in this direction.

In the reference T configuration shown in Fig.5.d, the direction L is now normal to the figure. Displacements are imposed in the T-direction on the (L,S) boundaries, which corresponds to simple tension along the T-direction, also with quasi-static applied strain rate $10^{-4}s^{-1}$. The (L,T) boundaries of the slab are still free surfaces. Periodic conditions are now imposed on the external (S,T) boundaries, and plane-strain normal to the L direction is assumed, with only a thin slice of material considered in this direction. The grain and slab thicknesses are unchanged, the slab length in the direction of loading is still $114\mu m$, but it now involves four grains of equal length. Hence, the main morphological difference between the L and T loading conditions is that the grains are shorter in the loading direction in the T configuration. Grain boundaries normal to the loading direction are now involved, in contrast with the L configuration.

From these two reference configurations, samples with reduced thickness are produced in two different ways, to mimic the experimental processing routes described in Section 2. First, as shown in Figs. 5.b,e, the slab thickness is reduced by decreasing the number of through-thickness grains, while keeping their dimensions l, t, s constant. Thus, the slab thickness $S = 54\mu m$ now involves only 9 grains of thickness $s = 6\mu m$, instead of 19. This is assumed to be representative of reducing the sheet thickness by machining. Second, as shown in Figs. 5.c,f, the slab thickness is reduced by decreas-

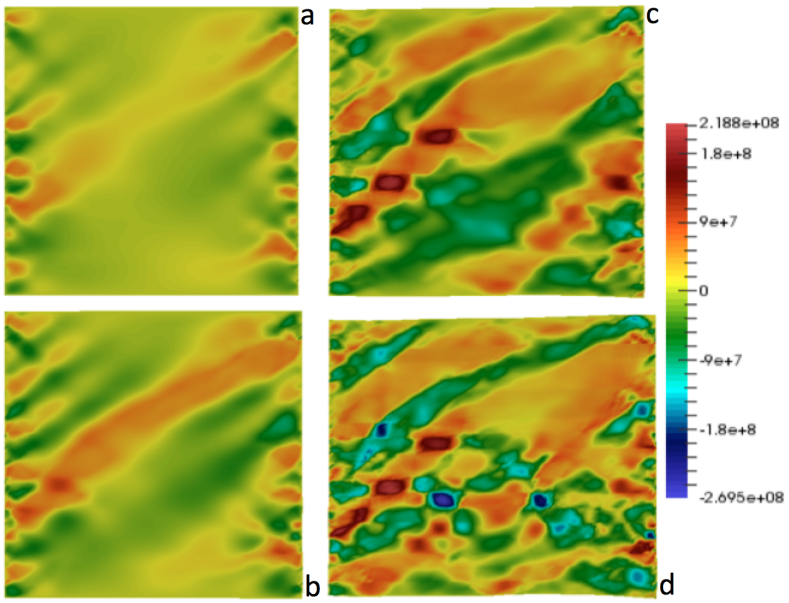

Figure 6: Simulated in-plane shear stress field in the L-S cross-section (Pa) at progressive strains of (a) 1%, (b) 2%, (c) 5% and (d) 10% in simple tension along direction L for the reference configuration shown in Fig.5.a. L direction is horizontal, S is vertical.

ing the grain thickness s, while keeping the number of through-thickness grains constant. The grain thickness is now $s = 3\mu m$, and the total slab thickness is therefore $S = 57\mu m$. This is assumed to be representative of reducing sheet thickness by adding rolling passes. For all samples shown in Fig.5, the initial orientation map is randomly made of grain orientations representative of the experimental texture components shown in Table 1. The distribution is mainly composed of S and brass orientations. The simulations were performed by using the open-source finite element software FreeFem++ (Hecht,2012; Hecht,2016). We used tetrahedral elements with quadratic interpolation for the displacements, six tetrahedrons building a cube of edge length $1\mu m$. We employed either 57 or 114 such cubes in the through-thickness direction S and 114 in the loading direction, which yielded meshes comprising either 38988 or 77996 elements.

We first analyze the simulation results for the L configuration shown in Fig.5.a with enforced tangential continuity of the elastic/plastic distortion

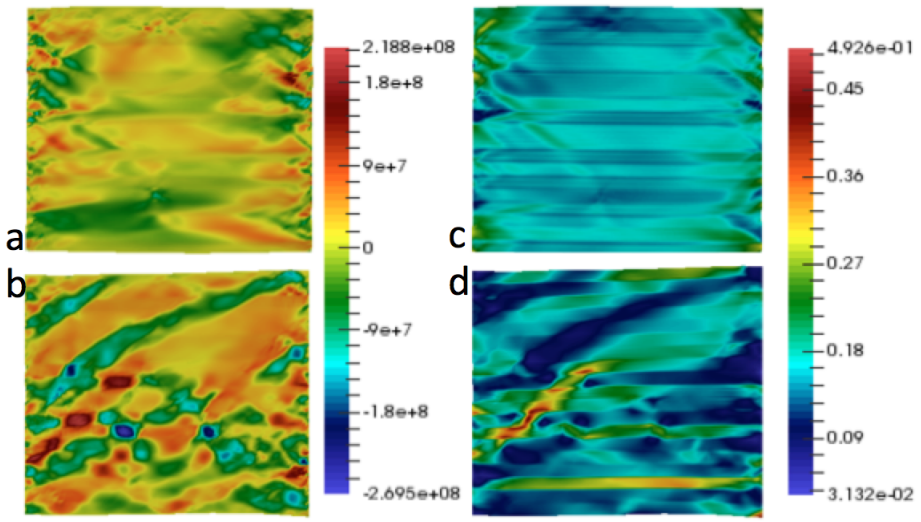

Figure 7: Simulation results in the L-S cross-section at a strain of 10% in simple tension in the direction L for the reference configuration shown in Fig.5.a. L direction is horizontal, S is vertical. Left: (a) in-plane shear stress field (Pa) without tangential continuity conditions, (b) with tangential continuity conditions implemented. Right: Effective strain field, (c) without tangential continuity conditions, (d) with tangential continuity conditions implemented.

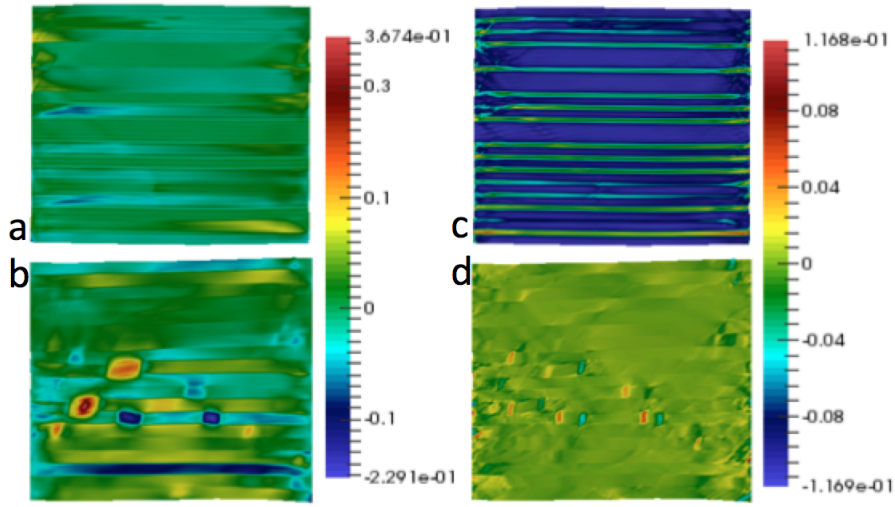

Figure 8: Simulation results in the L-S cross-section at a strain of 10% in simple tension in the direction L for the reference configuration shown in Fig.5.a. L direction is horizontal, S is vertical. Left: in-plane plastic shear strain field, (a) without tangential continuity conditions, (b) with tangential continuity conditions implemented. Right: Geometrically necessary dislocation density field (c) without tangential continuity conditions (norm $\sqrt{\alpha_{ij}\overline{\alpha_{ij}}}$, maximum values in red are $0.3\mu_m^{-1}$), and (d) with tangential continuity conditions implemented (component $\alpha_{LS}(\mu_m^{-1})$).

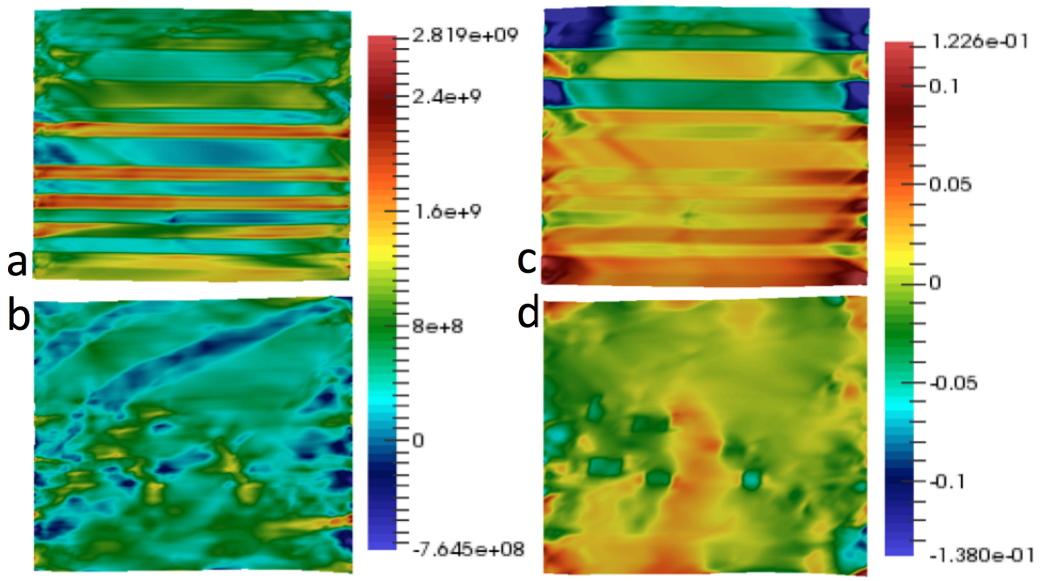

Figure 9: Simulation results in the L-S cross-section at a strain of 10% in simple tension in the direction L for the reference configuration shown in Fig.5.a. L direction is horizontal, S is vertical. Left: hydrostatic stress field (Pa) (a) without tangential continuity conditions, (b) with tangential continuity conditions implemented. Right: deformation-induced elastic rotation about the axis perpendicular to the figure (radians), (c) without tangential continuity conditions, (d) with tangential continuity conditions implemented.

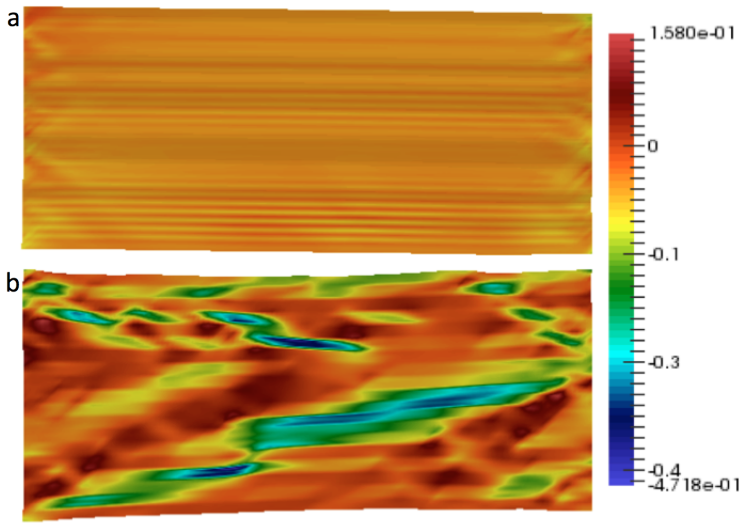

Figure 10: Simulation results in the L-S cross-section at 10% applied strain in simple tension in the direction L for the configuration shown in Fig.5.c. L direction is horizontal, S is vertical. Strain field ϵ_{22}, (a) in the absence of tangential continuity conditions, (b) with tangential continuity conditions implemented.

rate. In particular, Eq.31 implies continuity of the tensile plastic strain rate, $[\![\dot{\epsilon}^p_{11}]\!] = 0$, along all interfaces. The evolution of the in-plane shear stress field, or equivalently the elastic in-plane shear strain field, with increasing applied tensile strain is shown in Fig.6. Additionally, the total effective strain field can be seen in Fig.7.d, the in-plane plastic shear strain field in Fig.8.b and the dislocation density field in Fig.8.d at 10% strain. As is apparent in Fig.6.a at 1% strain, localization of the elastic shear strain occurs at the early stages of the deformation process in different regions ("hot spots") of the sample. Due to nonlocal interactions, these hot spots quickly percolate and merge into a single slanted shear band extending throughout the sample (see Fig.6.b at 2% strain), while other slanted shear bands start to develop. At the larger strains 5% and 10%, it is seen in Figs. 6.c,d,7.b,8.b that more intense hot spots of strong intragranular shear stress and plastic shear strain show up within the first band. In our simulations, the corresponding grains have been identified as having brass-a (positive shear strain) and S-a (negative shear strain) orientations. In Fig.7.d, the effective strain reaches 50% near these hot spots, at 10% applied strain. This is suggesting that these

orientations are favorable to shear strain localization. The above predictions are in excellent qualitative agreement with the experimental maps of incremental effective strain fields reported in (Morgeneyer,2014).

In Figs. 7-10, the above results are now compared with conventional CPFE calculations for the same initial configurations, where we recall that tangential continuity of the plastic distortion rate is not implemented. In Fig.7, the in-plane shear stress and effective strain fields are compared at 10% strain. From Fig.7.a,b, it is seen that the shear stress field is much more homogeneous when tangential continuity is overlooked. Fig.7.c,d shows that this trend is even stronger in the total effective strain field. It is also instructive to compare the predicted plastic shear strain and dislocation density fields with or without tangential continuity implemented. Fig.8 shows these fields at a strain of 10%. When tangential continuity is overlooked (see Fig.8.a,c), the plastic shear strain field evolves rather homogeneously and independently within each grain. As a result, the predicted dislocation density field, which is obtained in that case from the steps $(\mathbf{1},\mathbf{2})$ in the above algorithm, reduces almost exclusively to the surface dislocations accommodating the incompatibility between the granular plastic shear strain fields. In contrast, enforcing tangential continuity (Fig.8.b,d) leads to the a much more heterogeneous plastic strain field. Further, the dislocation density field ceases to be interfacial and grain-wise homogeneous. Interestingly, dislocation walls emerge and build transverse sub-grain boundaries within grains of brass-a and S-a orientation to accommodate the strong plastic strain localization hot spots occurring within the shear band. Fig.9 shows the influence of tangential continuity on the hydrostatic stress and elastic rotation fields at 10% strain. Again, without continuity conditions (Fig.9.a.c), grain-wise homogeneous fields are observed to evolve almost independently of one another. Large rotations and strong hydrostatic stresses reaching positive values as high as $3GPa$ are obtained. Such stresses may be expected to favor delamination rather than slanted shear banding, a tendency at odds with experimental findings. In contrast, the hydrostatic stress field obtained when accounting for tangential continuity is heterogeneous at sample scale (see Fig.9.b) and localization bands of compressive hydrostatic stress are seen on top of the shear strain bands, which is expected to prevent delamination. This result is again consistent with the experimental observations of (Morgeneyer,2014) as well as ours, and it suggests the prevailing influence of shear banding in the eventual fracture process. Comparing Fig.9.c,d clearly

shows that tangential continuity has a very strong impact on the elastic rotation field. Using Eq.31, it can be shown that tangential continuity of the plastic distortion rate at grain boundaries implies continuity of the through-thickness plastic rotation rate component: $[\![\dot{\omega}_2^p]\!] = 0$. Thus, the $\dot{\omega}_2^p$ field, which is characterized by grain-wise homogeneity and trans-granular discontinuity in CPFE calculations, switches to intra-granular heterogeneity and trans-granular continuity, with the additional emergence of rotation patterns linked with local crystal orientation. The effects on texture evolution, not accounted for in the present simulations, are therefore expected to be significant, as was indeed shown in (Mach,2010). Finally, Fig.10 shows comparison of the transverse stretch fields ϵ_{22} at 10% applied strain for the reference configuration shown in Fig.5.c. It is seen in Fig.10.a that the ϵ_{22} field is rather homogeneous in the absence of tangential continuity. The sample is subject to slight bending, but no necking is visible. In contrast, Fig.10.b clearly shows a mild necking region featuring a localized strain band lying across the sample.

We now analyze the influence of sheet and grain thickness on shear strain localization in samples loaded in direction L. The predicted effective strain fields for the three configurations introduced in Fig.5.a,b,c are shown in Fig.11.a,b,c. In moving from Fig.11.a to Fig.11.b, the slab thickness is reduced by decreasing the number of through-thickness grains,while keeping constant the grain thickness. As already indicated, this is intended to mimic the reduction of the sample's thickness by machining. It is seen in Fig.11.b that the various strain localization areas do not percolate decisively throughout the sample. Note that, despite the likelihood of additional material work hardening stemming from the machining process, the initial dislocation density was not increased in the simulation. Such an increase would have further hindered the occurence of shear banding. In moving from Fig.11.a to Fig.11.c, the slab thickness is decreased by reducing both the grain and sample thickness. As already mentioned, this is assumed to mimic the reduction of the sample's thickness by an additional rolling pass. It is seen in Fig.11.c that strain localization is significantly enhanced, as a well-defined simply connected shear band with very large strain values is now seen crossing the entire sample, while necking can also be noticed. The negative transverse stretch field in this band was also shown in Fig.10.b above. We checked that enhancing the material work hardening by introducing an increase of the initial dislocation density in the simulation tends to hinder the development of shear strain localization. However, this trend is overwhelmed by

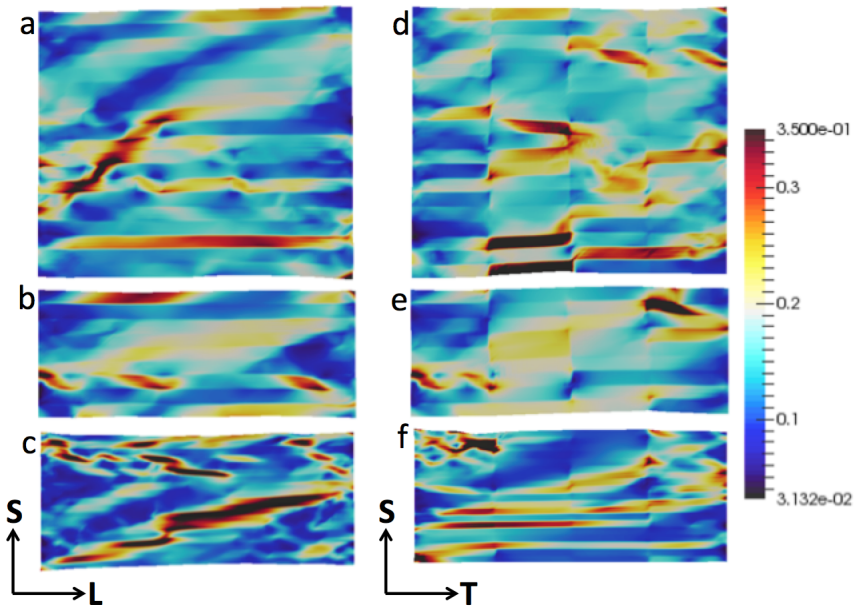

Figure 11: Predicted effective strain fields at 10% applied strain in simple tension for the different slab configurations shown in Fig.5. Left : tension along L direction of a slab with (a) 19 grains of thickness $6\mu m$, (b) 9 grains of thickness $6\mu m$ and (c) 19 grains of thickness $3\mu m$. The rolling frame is shown at the bottom. Right: tension along T direction of a slab with (d) 19 grains of thickness $6\mu m$, (e) 9 grains of thickness $6\mu m$ and (f) 19 grains of thickness $3\mu m$. The rolling frame is shown at the bottom.

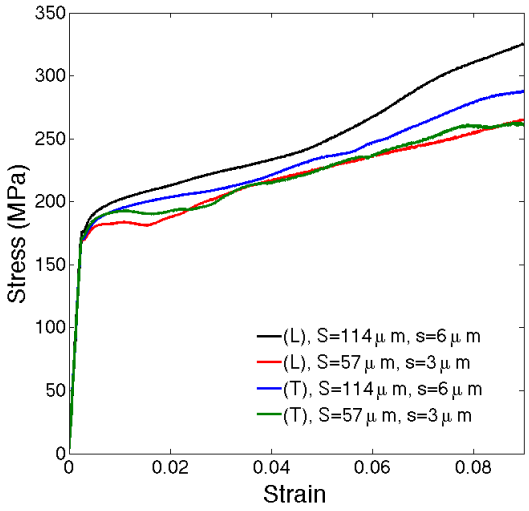

Figure 12: Simulated nominal stress vs. applied strain curves for configurations (a) and (c) (L loading, $6\mu m$ and $3\mu m$ grain thickness respectively) and (d,f) (T loading, $6\mu m$ and $3\mu m$ grain thickness respectively) in Fig.5. Tangential continuity enforced.

the opposite trend to strain localization when the dislocation density value amounts to what is expected from the additional rolling pass (no larger than a tenfold increase). Preventing the occurence of shear banding would require unrealistically high initial dislocation density values. This grain size effect is also apparent in the overall stress vs. applied strain response of the samples plotted in Fig.12. In this figure, the black and red curves are obtained for samples loaded in the L direction, for configurations (a,c) in Fig.5 corresponding to $6\mu m$ and $3\mu m$ grain thickness respectively, and for same initial dislocation densities. Both curves display work hardening but, nevertheless, necking and shear banding are observed in the simulations. The grain size effect is manifested in the relative softening of the behavior at small grain thickness, suggesting a sample more prone to localization. Summarizing the above results, it may be stated that increasing the density of surface area supporting tangential continuity per sample volume unit enhances strain localization, which suggests that the ductility of the sample will eventually be reduced. This is consistent with our experimental findings (trends (ii) and (iii)), where distinctly smaller elongation to failure is reported in loading in direction L when the samples are further rolled.

So far, we have found tangential continuity having a strong impact on strain localization in all L loading configurations. The origin of this behavior can be traced to the morphological texture shown in Fig.5.a,b,c. Because all interfaces are parallel to the loading direction L, the continuity constraint $[\![\dot{\epsilon}^p_{11}]\!] = 0$ on the tensile plastic strain rate is uniformly enforced on uninterrupted surfaces, which contributes decisively to the development of through-sample simply connected localization bands. Thus, it is now instructive to investigate the effects of the transverse interfaces (normal to the loading direction) appearing in the T configurations shown in Fig.5.d,e,f. Fig.11.d,e,f shows the predicted effective strain fields at 10% applied strain for these three configurations. Because normal discontinuity of the elastic and plastic distortion rates is allowed across interfaces, the transverse interfaces induce discontinuities $[\![\dot{\epsilon}^p_{11}]\!]$, and effectively act as barriers to the development of through-sample strain localization bands. This is clearly seen in Fig.11.d,e,f, where several strain localization regions are interrupted by transverse boundaries, so that percolation of shear banding throughout the body is prevented. Thus, in contrast to L configurations, T configurations tend to oppose or to limit strain localization, because the interfaces supporting tangential continuity of the tensile plastic strain rate $\dot{\epsilon}^p_{11}$ become fragmented. The effect of grain size previously seen in L configurations is still present, but much less noticeable, as Fig.12 also shows. In this figure, the blue and green curves represent the nominal stress vs. applied strain behavior when loading the samples in the T direction, with grain thicknesses $6\mu m$ and $3\mu m$ corresponding to configurations (d,f) in Fig.5 respectively, and with same initial dislocation density as the black and red curves. It is seen that the relative softening tendency that results from decreasing the grain size is smaller in the T direction than in the L direction (black and red curves). Thus, transverse boundaries act as strain localization inhibitors at all grain sizes, although less prominently at small grain sizes. Interpreting shear bands as precursors to failure, as already discussed above, leads to expecting higher ductility in T loading than in L loading configurations. Again, this tendency is fully consistent with the experimental trends (i) and (iii) revealed by our data.

7. Summary and concluding remarks

In the present paper, tangential continuity of the plastic distortion rate along grain boundaries is appended to an otherwise standard CPFE framework to perform tensile simulations of thin polycrystalline Al-Cu-Li samples with a strongly anisotropic multi-layered microstructure. As a result, the mechanical framework is rendered nonlocal. In contrast with most nonlocal gradient plasticity theories, the material properties do not involve any explicit dependence on grain size or on any other phenomenological internal length scale. Non-locality of the mechanical behavior of the polycrystal actually derives from the removal of undue plastic incompatibility along grain boundaries. Because dislocations induce $1/r$ variations of the elastic fields (Hirth,1982), where r is the distance from the dislocation, removing undue interfacial dislocations to satisfy tangential continuity of the plastic distortion rate introduces $1/r$ long-range interactions across the grain boundaries. The most striking outcome of the enforcement of tangential continuity is the occurrence of slanted through-sample shear banding, which standard CPFE calculations fail to predict. Such predictions are consistent with experimental observations of shear bands in Al-Cu-Li alloys in (Morgeneyer,2014) and in our own experiments. Moreover, enforcing the tangential continuity conditions on the plastic distortion rate allows explaining several observed trends on size and orientation effects: (i) decreasing grain thickness by further rolling the samples enhances strain localization, because the volumetric density of interfaces supporting tangential continuity is increased, (ii): loading the sample in the transverse direction T hinders strain localization, because the interfaces supporting tangential continuity of the tensile plastic strain rate become interrupted by transverse interfaces. The strongly anisotropic morphological texture of the present Al-Cu-Li alloys is clearly a key requirement for obtaining such conclusions. Therefore, similar results may also be obtained from this model in other materials with anisotropic morphological texture.

We now try to infer from the above analyses how the present predictions could be improved and extended in future work. We believe that forthcoming studies of plastic strain localization and fracture in Al-Cu-Li sheet samples should develop along four different axes.(i) The industrial sheet products involve much more grains in the through-thickness direction than can be dealt with in reasonable computing times by the present finite element framework.

However, considering large polycrystalline aggregates would allow refining the present predictions and perhaps retrieving experimental observations more closely. In this aim, parallel computing, advanced algorithms and specialized computer hardware (Knezevic,2014b), as well as spectral methods encompassing tangential continuity requirements could be useful, because they would significantly reduce computing times. Spectral methods using Fast Fourier Transform (FFT) techniques are presently under development in our group. In particular, the implementation of tangential continuity conditions requires solving Poisson-type equations to correct the plastic distortion, a problem already solved by such techniques in (Berbenni,2014). (ii) Solute and precipitate conditions should be accounted for, because dynamic aging of dislocations by diffusing solute atoms may induce strain rate softening and the Portevin - Le Chatelier effect. The resulting instability of the homogeneous plastic flow may well promote strain localization as discussed in a similar context in (Kok,2003), and have significant implications on ductility and failure (Delafosse,1993). (iii) The dislocation density fields predicted from the present framework and shown above in Fig.8.d, are obtained from purely elasto-static equations. Allowing these dislocation fields to move in their own stress field and in the applied stress field as in the Field Dislocation Mechanics theory (FDM) (Acharya,2001) would allow up-dating these dislocation configurations and the plastic distortion rate, with yet unknown consequences on material behavior and strain localization. For instance, in addition to the additional stretching step applied in the rolling direction, the anisotropy of dislocation transport might contribute to the increase of the UTS shown in Fig.2 when the loading direction switches from T to L direction. Indeed, in T loading, the plastic tensile elongation rate $\dot{\epsilon}^p_{11}$ derives from the motion of edge dislocations gliding on their slip planes in the (L,S) rolling and through-thickness directions. The mean free path of these dislocations is limited in the latter direction, due to grain boundaries acting as obstacles to dislocation motion, but unlimited from this point of view in the former direction. Conversely, in L loading, $\dot{\epsilon}^p_{11}$ derives from the motion of edge dislocations in the (S,T) through-thickness and transverse directions, which are both limited by grain boundary barriers. Hence, plastic flow should be more difficult in L loading than in T loading, consistent with the corresponding TYS/UTS increase. Such a conjecture could be verified using the FDM framework, inasmuch as the treatment of tangential continuity of the plastic distortion rate allows managing dislocation pile-up/transfer at grain boundaries. (iv) Beyond the present investigation of strain localization phenomena

in multi-layered polycrystals, concurrent modeling of the elasto-plastic interactions between dislocations and cracks is needed if one is to understand the nucleation and growth of cracks from pre-existing shear bands, and to quantitatively describe the transition from strain localization to fracture. Such a task will be attempted in forthcoming work by using the coupled theory for plasticity and fracture introduced in (Fressengeas,2014; Fressengeas,2016).

References

[Acharya,2001] A. Acharya, *A model of crystal plasticity based on the theory of continuously distributed dislocations*, J. Mech. Phys. Solids, **49**, 761-784 (2001).

[Acharya,2004] A. Acharya, *Constitutive analysis of finite deformation field dislocation mechanics*, J. Mech. Phys. Solids, **52**, 301-316 (2004).

[Acharya,2007] A. Acharya, *Jump condition for GND evolution: a connection between grain growth and slip transmission at grain boundaries*, Phil. Mag. **87**, 1349-1359 (2007).

[Alexopoulos,2013] N.D. Alexopoulos, E. Migklis, A. Stylianos, D.P. Myriounis, *Fatigue behavior of the aeronautical Al-Li (2198) aluminum alloy under constant amplitude loading*, Int. J. Fatigue **56**, 95-105 (2013).

[Ardeljan,2015] M.Ardeljan, M. Knezevic, T. Nizolek, I.J. Beyerlein, N.A. Mara, T.M. Pollock, *A study of microstructure-driven strain localizations in two-phase polycrystalline HCP/BCC composites using a multi-scale model*, Int. J. Plasticity, **74**, 35-57 (2015).

[Beaudoin,2013] A.J. Beaudoin, M. Obstalecki, W. Tayon, M. Hernquist, R. Mudrock, P. Kenesei, U. Lienert, *In situ assessment of lattice strain in an Al-Li alloy*, Acta Mater. **61**, 3456-3464 (2013).

[Berbenni,2014] S. Berbenni, V. Taupin, K.S. Djaka, C. Fressengeas, *A numerical spectral approach for solving elasto-static field dislocation and g-disclination mechanics*, Int. J. Solids Structures **51**, 4157-4175 (2014).

[Besson,2001] J. Besson, D. Steglich, W. Brocks, *Modeling of crack growth in round bars and plane strain specimens*, Int. J. Solids Structures **38**, 8259-8284 (2001).

[Bilby,1955] B.A. Bilby, Types of dislocation sources, in: Bristol Conference Report on Defects in Crystalline Solids, The Physical Society, London, 124 (1955).

[Broek,1974] D. Broek, Elementary Engineering Fracture Mechanics, Noordhoff International Publishing (1974).

[Chen,2011] J. Chen, Y. Madi, T.F. Morgeneyer and J. Besson, *Plastic flow and ductile rupture of a 2198 AlCuLi aluminum alloy*, Comp. Mat. Sci. **50**, 1365-1371 (2011).

[Csiszár,2011] G. Csiszár, A. Misra, T. Ungár, *Burgers vector types and the dislocation structures in sputter-deposited Cu-Nb multilayers*, Mat. Sci. Eng. A **528**, 6887-6895 (2011).

[Delafosse,1993] D. Delafosse, G. Lapasset, L.P. Kubin, *Dynamic strain-aging and crack propagation in the 2091 Al-Li alloy*, Scripta Metall. Mater. **29**, 1379-1384 (1993).

[Frank,1950] F.C. Frank, The resultant content of dislocations in an arbitrary intercrystalline boundary, in: Symposium on The Plastic Deformation of Crystalline Solids, Mellon Institute, Pittsburgh, (NAVEXOS-P-834), 150 (1950).

[Fressengeas,2012] C. Fressengeas, V. Taupin, L. Capolungo, M. Upadhyay, *Tangential continuity of elastic/plastic curvature and strain at interfaces*, Int. J. Solids Structures, **49**, 2660-2667 (2012).

[Fressengeas,2014] C. Fressengeas, V. Taupin, *A field theory of distortion incompatibility for coupled fracture and plasticity*, J. Mech. Phys. Solids **68**, 45 (2014).

[Fressengeas,2016] C. Fressengeas, V. Taupin, *A field theory of strain/curvature incompatibility for coupled fracture and plasticity*, Int. J. Solids Structures **82**, 16-38 (2016).

[Hadamard,1903] J. Hadamard, Leçons sur la propagation des ondes et les équations de l'hydrodynamique, Herman, Paris (1903).

[Hecht,2012] F. Hecht, *New development in FreeFem++*, J. Numer. Math. **20**, 251-265 (2012).

[Hecht,2016] F. Hecht, O. Pironneau, A. Le Hyaric, K. Ohtsuka, freefem++, www.freefem.org/ff++/

[Heinz,2000] A. Heinz, A. Haszler, C. Keidel, S. Moldenhauer, R. Benedictus, *Recent development in aluminium alloys for aerospace applications*, W.S. Miller, Mater. Sci. Eng. A **280**, 102-107 (2000).

[Hirth,1982] J.P. Hirth, J. Lothe, Theory of Dislocations, 2nd ed. Wiley, New York (1982).

[Knezevic,2014a] M. Knezevic, B. Drach, M. Ardeljan, I.J. Beyerlein, *Three dimensional predictions of grain scale plasticity and grain boundaries using crystal plasticity finite element models*, Comput. Methods Appl. Mech. Engrg. **277**, 239-259 (2014).

[Knezevic,2014b] M. Knezevic, D.J. Savage, *A high-performance computational framework for fast crystal plasticity simulations*, Comp. Mat. Sci. **83**, 101-106 (2014).

[Kok,2003] S. Kok, M.S. Bharathi, A.J. Beaudoin, C. Fressengeas, G. Ananthakrishna, L.P. Kubin, M. Lebyodkin, *Spatial coupling in jerky flow using polycrystal plasticity*, Acta Mater. **51**, 3651-3662 (2003).

[Kröner,1980] E. Kröner, Continuum theory of defects. In: Balian, R. (Ed.), Les Houches, Session XXXV. Physics of Defects. North-Holland, Amsterdam, 217-315 (1980).

[Lavernia,1987] E.J. Lavernia, N.J. Grant, *Aluminum Lithium alloys*, J. Mater. Sci. **22**, 1521-1529 (1987).

[Mach,2010] J. Mach, A.J. Beaudoin, A. Acharya, *Continuity in the plastic strain rate and its influence on texture evolution*, J. Mech. Phys. Solids **58**, 105 (2010).

[Messner,2014] M.C. Messner, A.J. Beaudoin, R.H. Dodds Jr., *Mesoscopic modeling of crack arrestor delamination in Al-Li: primary crack shielding and -stress effect B*, Int. J. Fract. **188**, 229-249 (2014).

[Messner,2015] M.C. Messner, A.J. Beaudoin, R.H. Dodds Jr., *An interface compatibility/equilibrium mechanism for delamination fracture in aluminum-lithium alloys*, Eng. Fract. Mech. **133**, 70-84 (2015).

[Morgeneyer,2011] T.F. Morgeneyer, J. Besson, *An interface compatibility/equilibrium mechanism for delamination fracture in aluminum-lithium alloys*, Scripta Mater. **65**, 1002-1005 (2011).

[Morgeneyer,2014] T.F. Morgeneyer, T. Taillandier-Thomas, L. Helfen, T. Baumbach, I. Sinclair, S. Roux, F. Hild, *In situ 3-D observation of early strain localization during failure of thin Al alloy (2198) sheet*, Acta Mater. **69**, 78-91 (2014).

[Nye,1953] J.F. Nye, *Some geometrical relations in dislocated crystals*, Acta Metall., **1**, 153-162 (1953).

[Ovri,2015a] H. Ovri, E.A. Jägle, A. Stark, E.T. Lilleodden, *Microstructural influences on strengthening in a naturally aged and overaged Al-Cu-Li-Mg based alloy*, Mater. Sci. Eng. A **637**, 162-169 (2015).

[Ovri,2015b] H. Ovri, E.T. Lilleodden, *New insights into plastic instability in precipitation strengthened Al-Li alloys*, Acta Mater. **89**, 88-97 (2015).

[Priester,1979] L. Priester, R.W. Balluffi, *Technique for studying the interaction of lattice dislocations with grain boundaries during plastic deformation*, J. Micros. Spectrosc. Electr. **4**, 615-622 (1979).

[Priester,2013] L. Priester, *Grain boundaries From Theory to Engineering*, Springer Series in Materials Science, 172 (2013).

[Puri,2011] S. Puri, A. Das, A. Acharya, *Mechanical response of multicrystalline thin films in mesoscale field dislocation mechanics*, J. Mech. Phys. Solids **59**, 2400-2417 (2011).

[Richeton,2011] T. Richeton, G.F. Wang, C. Fressengeas, *Continuity constraints at interfaces and their consequences on the work hardening of metal-matrix composites*, J. Mech. Phys. Solids **59**, 2023-2043 (2011).

[Warner,2006] T. Warner, *Recently-developed aluminium solutions for aerospace applications*, Mat. Sc. Forum , **519-521** 1271-1278 (2006)

[Taupin,2015] V. Taupin, L. Capolungo, C. Fressengeas, M. Upadhyay, B. Beausir, *A mesoscopic theory of dislocation and disclination fields for grain boundary-mediated crystal plasticity*, Int. J. Solids Structures **71**, 277-290 (2015).

[Xue,2007] L. Xue, *Damage accumulation and fracture initiation in uncracked ductile solids subject to triaxial loading*, Int. J. Solids Structures **44**, 5163-5181 (2007).

[Zhang,2014] S.F. Zhang, W.D. Zeng, W.H. Yang, C.L. Shi, H.J. Wang, *Damage accumulation and fracture initiation in uncracked ductile solids subject to triaxial loading*, Mater. Design **63**, 368-374 (2014).

Appendix A. Mathematical notations

A bold symbol denotes a tensor. When there may be ambiguity, an arrow is superposed to represent a vector: $\vec{\mathbf{V}}$. The symmetric part of tensor $\mathbf{A}$ is denoted $\mathbf{A}^{sym}$. Its skew-symmetric part is $\mathbf{A}^{skew}$ and its transpose is denoted by $\mathbf{A}^t$. The tensor $\mathbf{A}\cdot\mathbf{B}$, with rectangular Cartesian components $A_{ik}B_{kj}$, results from the dot product of tensors $\mathbf{A}$ and $\mathbf{B}$, and $\mathbf{A}\otimes\mathbf{B}$ is their tensorial product, with components $A_{ij}B_{kl}$. The vector $\mathbf{A}\cdot\mathbf{V}$, with rectangular Cartesian components $A_{ij}V_j$, results from the dot product of tensor $\mathbf{A}$ and vector $\mathbf{V}$. A : represents the trace inner product of the two second order tensors $\mathbf{A}:\mathbf{B}=A_{ij}B_{ij}$, in rectangular Cartesian components, or the product of a higher order tensor with a second order tensor, e.g., $\mathbf{A}:\mathbf{B}=A_{ijkl}B_{kl}$. The cross product of a second-order tensor $\mathbf{A}$ and a vector $\mathbf{V}$, the **div** and **curl** operations for second-order tensors are defined row by row, in analogy with the vectorial case. For any base vector $\mathbf{e}_i$ of the reference frame:

$$(\mathbf{A}\times\mathbf{V})^t\cdot\mathbf{e}_i = (\mathbf{A}^t\cdot\mathbf{e}_i)\times\mathbf{V} \quad (32)$$

$$(\mathbf{div}\ \mathbf{A})^t\cdot\mathbf{e}_i = \mathbf{div}(\mathbf{A}^t\cdot\mathbf{e}_i) \quad (33)$$

$$(\mathbf{curl}\ \mathbf{A})^t\cdot\mathbf{e}_i = \mathbf{curl}(\mathbf{A}^t\cdot\mathbf{e}_i). \quad (34)$$

In rectangular Cartesian components:

$$(\mathbf{A}\times\mathbf{V})_{ij} = e_{jkl}A_{ik}V_l \quad (35)$$

$$(\mathbf{divA})_i = A_{ij,j} \quad (36)$$

$$(\mathbf{curlA})_{ij} = e_{jkl}A_{il,k}. \quad (37)$$

where e_{jkl} is a component of the third-order alternating Levi-Civita tensor. In the component representation, the spatial derivative with respect to a Cartesian coordinate is indicated by a comma followed by the component

index. A superposed dot represents a material time derivative.